metals

MDPI

Article

The Effects of a Submerged Entry Nozzle on Flow and Initial Solidification in a Continuous Casting Bloom Mold with Electromagnetic Stirring

Qing Fang, Hongwei Ni *, Hua Zhang, Bao Wang and Zean Lv

The State Key Laboratory of Refractories and Metallurgy, Wuhan University of Science and Technology, Wuhan 430081, China; qfang525@sina.com (Q.F.); huazhang@wust.edu.cn (H.Z.); wangbao1983@wust.edu.cn (B.W.); lvzean@163.com (Z.L.)
* Correspondence: nihongwei@wust.edu.cn; Tel.: +86-27-6886-2811

Academic Editor: Mohsen Asle Zaeem
Received: 24 February 2017; Accepted: 17 April 2017; Published: 19 April 2017

Abstract: The melt flow, level fluctuation, temperature field, and solidification behavior coupled with electromagnetic stirring (EMS) effects in the continuous casting mold region of U71Mn steel bloom were numerically analyzed by commercial computational fluid dynamics (CFD) software named ANSYS FLUENT. The effects of submerged entry nozzle (SEN) structures and the installation methods for optimized four-port SEN on the flow pattern, level fluctuation, heat transfer and initial solidification behavior in a bloom mold loaded with EMS were investigated. The aim is to propose a better SEN condition for the big bloom casting of high railway steel. The water simulation experiments were conducted to show the flow characteristics under different SEN conditions and verify the numerical model of flow pattern. The experimental and numerical simulation results showed that the optimized four-port SEN with diagonal installation cannot only improve the flow pattern of the molten steel by alleviating the level fluctuation and reducing the impact pressure to the wall. It is also beneficial for temperature variation at both bloom surface and corner, as well as the local solidified shell thinning phenomena due to the elimination of impingement effect.

Keywords: bloom mold; numerical simulation; submerged entry nozzle; flow pattern; solidified shell

1. Introduction

The big bloom continuous caster is widely used to produce high-end steel products, such as heavy rail steel, bearing steel and free-cutting steel. Most defects affecting steel quality in the continuous casting (CC) process are associated with metallurgical behavior in the mold, which is largely determined by the submerged entry nozzle (SEN). The SEN can affect the flow pattern, solidified shell growth, free surface status and inclusion removal in the CC mold [1,2]. Previous works have developed both experimental and numerical models for analyzing the flow [3–5] and initial solidification [6–8] in the CC mold under different SEN conditions. These studies found that an appropriate SEN structure cannot only enhance the flow field, but also improve the heat transfer process in the mold of both slabs and blooms significantly. To ensure good mold metallurgical behavior during a big bloom casting process, a proper type of SEN should be proposed and investigated.

At present, the SEN with straight single outlet is unfavorable for flotation removal of non-metallic inclusions and may lead to inactive meniscus. The two-port SEN may cause the solidified shell thinning at the narrow face, but can obtain a high removal rate of inclusions. Both types of SENs are widely applied for bloom castings. Recently, quad-furcated SENs with outlets perpendicular to the mold wall has become a concern with regard to which can alleviate level fluctuation and non-uniform solidification, and improve the removal rate of inclusions. Wu et al. [9] analyzed the metallurgical differences among the three kinds of SEN mentioned above, and found that four-port SEN is beneficial to both initial solidification and inclusion floating. Dang et al. [10] proposed a five-port SEN and compared with the four-port SEN. The new SEN can eliminate the non-uniform growth of solidifying shell and ensure flow stability. Sun et al. [11,12] designed a quad-furcated SEN with outlets at tangential directions to enhance the flow pattern by generating swirling flow and eliminating the non-uniform growth of solidified shell. This type of SEN has a complex structure, and may easily trigger nozzle clogging. The proper SEN structure for bloom casting is becoming multi-port, however it should not be too complicated. Therefore, the four-port SEN needs deeper investigation to obtain maximum metallurgical benefit. Meanwhile, as a widely applied technology for big bloom casting, in-mold electromagnetic stirring (M-EMS) affects the flow and solidification behavior in the bloom mold significantly. Ren et al. [13,14] investigated the flow and solidification process in the bloom mold with EMS under normal one-port SEN and found EMS can eliminate the superheat and weaken the immersion depth. To investigate the flow, heat transfer, and initial solidification process in the bloom mold under different SEN conditions more precisely, the effects of M-EMS should not be ignored.

The two-port SENs were formerly applied for the bloom casting of high rail steel U71Mn produced by the 3# con-caster in No. 1 Steelmaking Plant of Wuhan Iron & Steel Corporation (WISCO), where the slag entrapment and disqualification of non-metallic inclusions frequently occurred during the casting process. To solve this problem, an optimized four-port SEN with certain divergent and downward angle was designed to reduce the impingement effect of jet flow to the mold wall. Furthermore, researchers proposed a new idea to change the installation method of the optimized SEN from conventional orthogonal with outlets in the directions of mold wall centers to diagonal with outlets pointing at the mold corners. To prove the exact metallurgical advantage of the diagonally installed four-port SEN over others, the metallurgical differences in the bloom mold under the SENs of two-port, four-port with orthogonal and four-port with diagonal were discussed and compared in this paper. Water model experiments without EMS were conducted to discuss the basic difference of the flow pattern under the different SEN conditions to verify the applicability of the numerical turbulence model. Furthermore, the flow pattern, level fluctuation, heat transfer and initial solidification under different SENs were investigated and compared by a mathematical model considering the effect of M-EMS.

2. Model Descriptions

2.1. Basic Assumptions

In order to simulate the thermal-physical phenomena in continuous casting bloom mold, the following assumptions are made in the formulating of models:

(1) The turbulent flow and solidification phenomena of the steel in the mold are assumed to be at steady state.
(2) The influence of mold oscillation and mold taper is ignored.
(3) The molten steel is assumed to be homogeneous incompressible Newtonian fluid.
(4) Only the liquid slag layer is considered, other state slag layers are ignored.
(5) The curvatures of both mold and strand are not taken into account.

2.2. Governing Equations

2.2.1. Model of Fluid Flow

The flow pattern in the mold is numerically simulated by solving the continuity and momentum equations under turbulent conditions. The equations are as follows:

$$\frac{\partial(\rho u_i)}{\partial x_i} = 0 \qquad (1)$$

$$\rho\frac{\partial u_i u_j}{\partial x_j} = \frac{\partial}{\partial x_j}\left[\mu_{eff}\left(\frac{\partial u_i}{\partial x_j} + \frac{\partial u_j}{\partial x_i}\right)\right] - \frac{\partial P}{\partial x_i} + \rho g_i + F_E + S_P + F_T \tag{2}$$

where P is the pressure and u_i is the flow velocity in direction i; ρ is the volume fraction average density; μ_{eff} is the effective viscosity coefficient, which is the sum of the laminar (μ_l) and turbulent (μ_t) viscosity. μ_t can be defined as

$$\mu_t = \rho \cdot f_\mu \cdot C_\mu \cdot \frac{k^2}{\varepsilon} \tag{3}$$

The low-Reynolds number k-ε turbulent model [15] is applied to describe the turbulence flow and solidification phenomena in the computational domain. The governing equations can be written as follows:

$$\frac{\partial(\rho k u_i)}{\partial x_i} = \frac{\partial}{\partial x_i}\left(\frac{\mu_{eff}}{\sigma_k}\frac{\partial k}{\partial x_i}\right) + G - \rho\varepsilon + \rho D + S_k \tag{4}$$

$$\frac{\partial(\rho\mu_l\varepsilon)}{\partial x_j} = \frac{\partial}{\partial x_j}\left(\frac{\mu_{eff}}{\sigma_\varepsilon}\frac{\partial\varepsilon}{\partial x_j}\right) + C_\mu\frac{\varepsilon}{k}G - C_2 f_1\frac{\varepsilon}{k}\rho\varepsilon + \rho E + S_\varepsilon \tag{5}$$

where $S_k = \frac{\mu_l k}{K_P}$ and $S_\varepsilon = \frac{\mu_l \varepsilon}{K_P}$ are the solidification induced source terms; the empirical constants and functions in the low-Reynolds number model are presented in Table 1.

Table 1. Empirical constants and functions used in the Low-Reynolds number model.

C_2	σ_ε	σ_k	C-	f-	f_1	E	D	Re_t
1.92	1.3	1.0	0.09	$\exp\left[\frac{-3.4}{\left(1+\frac{Re_t}{50}\right)^2}\right]$	1	$2\frac{u\mu_t}{\rho}\left(\frac{\partial^2 u_i}{\partial x_j \partial x_k}\right)^2$	$2\mu\left(\frac{\partial(\sqrt{k})}{\partial x_i}\right)^2$	$\frac{\rho k^2}{\varepsilon}$

2.2.2. Heat Transfer Model

To obtain a precise prediction of the temperature field and solidification behavior of steel, the enthalpy equation is applied [16]:

$$\frac{\partial}{\partial t}(\rho_1 H) + \nabla\cdot(\rho_1 u H) = \nabla\cdot(\lambda\nabla T) \tag{6}$$

where λ and ρ_1 are the thermal conductivity and density of the steel, respectively, and u is the fluid velocity. The total enthalpy H can be described as

$$H = h_{ref} + \int_{T_{ref}}^{T} c_p dT + f_l L \tag{7}$$

where the c_p is specific heat, L is latent heat of molten steel solidification, and the liquid fraction f_l is updated by following formulations:

$$f_l = \frac{T - T_s}{T_l - T_s}\ (T_s < T < T_l) \tag{8}$$

2.2.3. Electromagnetism Model

The source term F_E in Equation (2) represents the electromagnetic force, which contains radial force ($\overline{F_r}$) and tangential force ($\overline{F_\theta}$) [17]:

$$\overline{F_r} = -\frac{1}{8}B_0^2\sigma^2\left(2\pi f - \frac{V_\theta}{r}\right)^2\mu_0 r^3 \tag{9}$$

$$\overline{F_\theta} = \frac{1}{2}B_0^2\sigma\left(2\pi f - \frac{V_\theta}{r}\right)r \tag{10}$$

where B_0 is the magnetic induction density at the boundary of molten steel; σ is the electrical conductivity of liquid steel; f is the current frequency of the EMS; V_θ is the tangential velocity; μ_0 is the magneto-conductivity; and r is the value of radial displacement. The radial force ($\overline{F_r}$) is ignored for $\overline{F_r}$, and is much smaller than $\overline{F}_\theta$ in a rotating magnetic field.

2.2.4. Effect of Phase Transfer

The source term of moment in Equation (2), S_P, which is called Darcy's source term, is utilized to account for the effect of phase change on the convection and turbulence in the mushy zone, which can be considered as porous medium. It can be described by the Darcy's law, the permeability K_p is presented as follows [18]:

Permeability parallel to primary dendrite arms:

$$K_p^{par} = \begin{cases} f_l < 0.7, \ [4.53 \times 10^{-4} + 4.02 \times 10^{-6} (f_l + 0.1)^{-5} \cdot \frac{\lambda_1^2 \cdot f_l^3}{1 - f_l} \\ f_l \geq \ 0.7, \ 0.07425 \cdot \lambda_1^2 \left[- \ln(1 - f_l) - 1.487 + 2(1 - f_l) - 0.5(1 - f_l)^2 \right] \end{cases} \tag{11}$$

Permeability perpendicular to primary dendrite arms:

$$K_p^{per} = \begin{cases} f_l < 0.7, \ 0.00173 \times \left(\frac{\lambda_1}{\lambda_2} \right)^{1.09} \times \frac{\lambda_2^2 \cdot f_l^3}{(1 - f_l)^{0.749}} \\ f_l \geq 0.7, \quad 0.03978 \cdot \lambda_1^2 [-ln f_s - 1.476 + 2 f_s - 1.774 f_s^2 + 4.076 f_s^3 \end{cases} \tag{12}$$

$$S_p = \frac{\mu_l}{K_p} (u_i - u_{s,\,i}) \tag{13}$$

where λ_1, λ_2 are the primary arm space and secondary arm space, respectively; and $u_{s,\,i}$ is the velocity of solid in the direction i.

In the calculations, the Darcy's source terms in three directions are calculated by Equation (13) and added into FLUENT calculations by User Defined Functions (UDF), in which K_p^{par} is applied in x and y direction, and K_p^{per} is used in z direction.

2.2.5. VOF Model

In this paper, the steel/slag interface fluctuation in the mold is tracked by volume of fluid (VOF) method which can model two or more immiscible fluids by solving a single set of momentum equations and tracking the volume fraction of each of the fluids throughout the domain. In the VOF model, for two kinds of fluids, a set of momentum equations are adopted in common; for incompressible fluid, it is assumed that the densities of liquid steel and slag are constant, so the volume fraction of liquid steel should conform to the following equation [16,19]:

$$\frac{\partial}{\partial x_i} (\alpha_{\mathrm{q}} u_i) = 0 \tag{14}$$

The primary-phase volume fraction will be computed based on the following constraint:

$$\sum_{q=1}^{n} \alpha_q = 1 \tag{15}$$

The volume fraction average density should be:

$$\rho = \sum_{q=1}^{n} \alpha_q \rho_q \tag{16}$$

where α_q means the phase fraction of q and ρ_q is the density of phase q. In this paper, the behavior of steel and slag interface is discussed, so the value of n is set to be 2. All other properties (for example, viscosity) are computed in this manner.

The surface tension source term in Equation (2), F_T, which is calculated by following equation:

$$F_T = 2\sigma_t \rho k_i \nabla \alpha_q / \sum_{q=1}^{n} \rho_q \tag{17}$$

where σ_t is the surface tension coefficient, and k_i is the curvature.

In the FLUENT algorithm, the geometric reconstruction scheme is used to describe the morphology of the phase interface [20].

3. Simulation Procedure

3.1. Simulation Models and Parameters

A quarter of three-dimensional (3D) schematics of the top part of the computational domain for the two-port SEN is given in Figure 1, in which the immersion depth of SEN is 210 mm, the thickness of slag film is 30 mm, and the distribution of the two phases can be obtained.

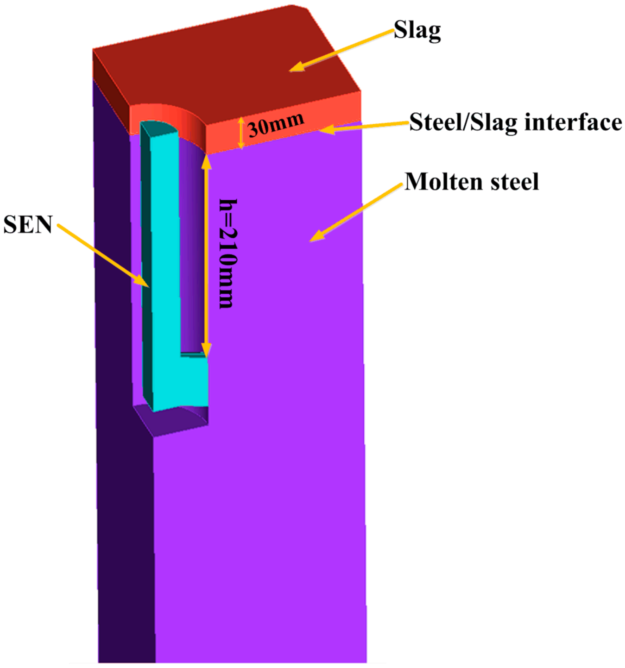

Figure 1. Top part of computational domain.

Full geometrical models are taken for all cases. For example, the meshed computational model equipped with the two-port SEN is shown in Figure 2, where the technology of local grid refinement is applied to simulate the behavior of the initial solidified shell more accurately. The meshes of FLUENT computational domain include non-uniform grids with approximately 1,700,000 cells. To better understand the effect of SEN structure and SEN installation on the metallurgical behavior in the CC bloom mold, water model experiments and numerical simulation cases under different SEN conditions are conducted in this paper. The SEN structures and install methods discussed in this paper are presented in Figure 3. In all SENs, the immersion depth, and nozzle outlet angle are fixed at 210 mm and 15°, respectively. Parallel calculations are performed on an Intel cluster using one node. Each calculation for different SEN conditions lasts about one day.

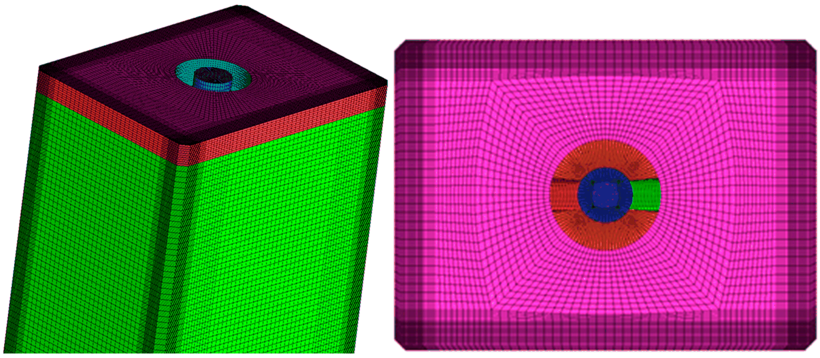

Figure 2. The meshed computational model equipped with two-port SEN and mold chamfer.

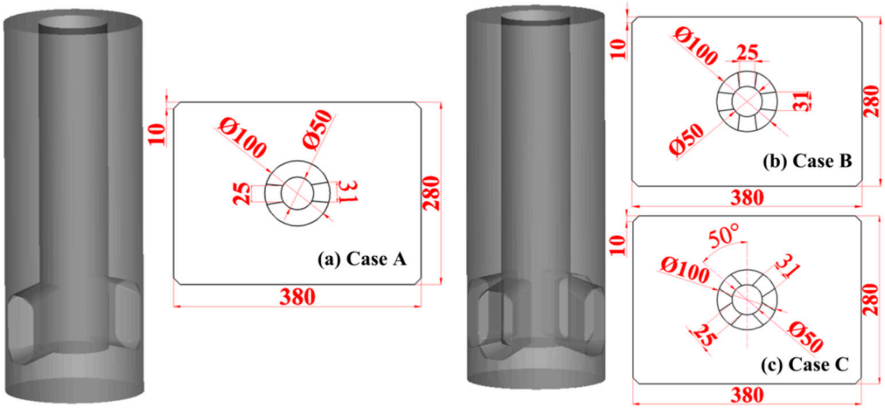

(a) A-type SEN (b) B-type SEN

Figure 3. (**a**,**b**) The geometric schematic of three types of the SENs and their installation methods.

The geometrical parameters and operation conditions of caster are summarized in Table 2. Table 3 lists the thermophysical properties of U71Mn steel and mold flux. As the slag in the upper part of the bloom mold does not participate in the solidification process, and the adiabatic condition is employed at the free surface, some of the slag thermophysical parameters are not necessary to this calculation. Viscosity and thermal conductivity are very important thermophysical parameters to predicting flow and solidification behavior of the steel, especially in the mushy zone. The variation of viscosity and thermal conductivity with local temperature are calculated by software code JMatPro7.0 (Sente Software Ltd., Surrey, UK) and applied in the calculation by piecewise linear form using the value points presented in Figure 4.

Table 2. Parameters and operating conditions.

Parameter	Value
Section size, mm^2	280 × 380
Mold length, mm	700
Casting speed, m/min	0.63
Calculation length, mm	1230
Casting temperature, K	1765.15
Water quantity in mold, L/min	2600
Thickness of slag film, mm	30
Current intensity of M-EMS, A	600
Operating frequency of M-EMS, Hz	2.0
EMS center, mm	420
Mold chamfer dimension, mm	10

Table 3. Thermal physical properties of U71Mn steel.

Parameter	**Value**
Density of steel, kg/m^3	7020
Density of slag, kg/m^3	2700
Viscosity of steel, Pa·s	Figure 4a
Viscosity of slag, Pa·s	0.2
Thermal conductivity of steel, J/(m·K·s)	Figure 4b
Specific heat, J/Kg/K	750
Solidus temperature, K	1643
Liquidus temperature, K	1737
Latent heat, J/kg	272,000
Electric conductivity, S/m	7.14×10^5
Steel/slag interface tension coefficient, N/m	1.4

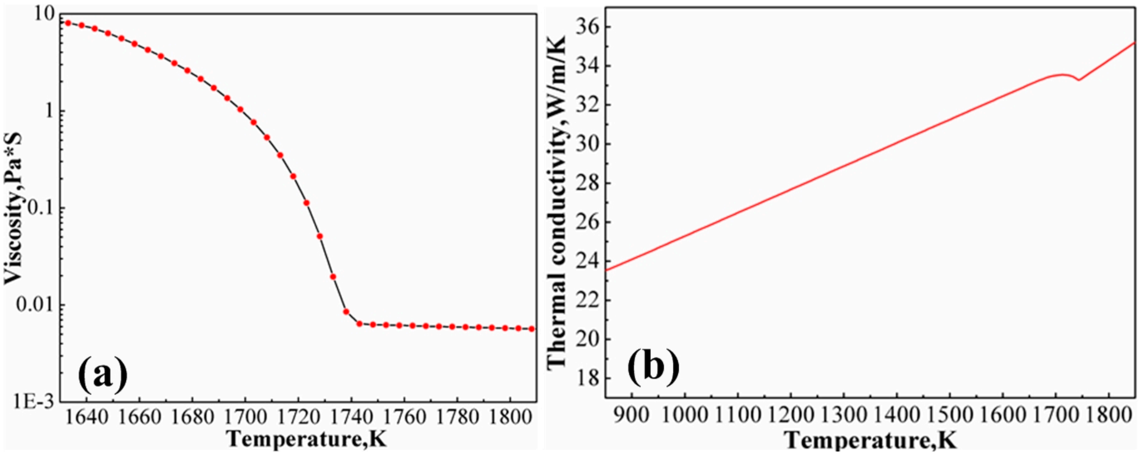

Figure 4. Variations of viscosity (**a**) and thermal conductivity (**b**) with local temperature.

3.2. Boundary and Initial Conditions

The initial and boundary conditions for velocity, turbulent kinetic energy and temperature are set according to set procedure. For inlet, $v_{in} = v_z = v_{cast} \times \frac{S_{mold}}{S_{SEN}} = 0.5679$ m/s, $v_x = v_y = 0$, $k_{in} = 0.01 v_{in}^2$, $\varepsilon = k_{in}^{1.5}/D$, $T_{in} = 1765.15$ K. It is noted that the k_{in} and ε are calculated by the semi-empirical equations [21]. For the computational outlet, the fully developed flow condition is applied, where the normal gradients of all variables are set to zero. For the free surface, the normal derivative of all variables is set to zero, and the adiabatic condition is employed at the free surface.

For the bloom wall, the detailed boundary conditions for heat transfer at the bloom wall are presented. In the mold region, the heat exchange effect in the domain is described by the average heat flux [22]:

$$\overline{q} = \frac{\rho_w \cdot c_w \cdot W \cdot \Delta T}{S} \tag{18}$$

where $\overline{q}$ is the average heat flux density, W/m^2; ρ_w is the density of cooling water, kg/m^3; c_w is specific heat capacity of cooling water, J/(kg·K); W is the flow rate of cooling water, m^3/s; ΔT is the water temperature difference in and out of cooling wall, K; and S is the effective contact area of liquid steel and mold wall, m^2. As the initial solidified shell is formed, the air gap between the mold copper and shell would lead to the uneven heat transfer of the steel bloom, reducing the heat flux of the corner [23]. In this work, a correction factor ($\alpha = 0.5$) of heat flux density on the corner ($\overline{q}_g$) is necessarily adopted while calculating the heat transfer behavior at the bloom corner:

$$\overline{q}_g = \alpha \cdot \overline{q} \tag{19}$$

when the bloom is pulled out of the mold, the heat transfer coefficient of zone I is calculated by following equation, in which water cooling is applied [24].

$$h = \beta \cdot 581 w^{0.541} (1 - 0.0075 T_w) \tag{20}$$

where h is the heat transfer coefficient at the bloom surface, $\mathrm{W}/\left(\mathrm{m}^2 \cdot \mathrm{K}\right)$; w is the spraying water density, $\mathrm{L}/\left(\mathrm{m}^2 \cdot \mathrm{s}\right)$; T_w represents the ambient temperature, K; and β is the correction factor of heat transfer coefficient in the secondary cooling zone.

3.3. Water Experiment and Flow Validation

There is no proper experimental method to validate EMS modeling. An indirect way could be the verification of its effect, for example, the amount of solidified shell in function of meniscus distance. In this paper, researchers conducted several water model experiments without EMS to obtain a brief understanding of the flow pattern in the mold under different SEN conditions and verify the numerical model without EMS. Subsequently, the electromagnetic force is calculated by Equation (10) and added into FLUENT by user defined functions as a momentum source to further investigate the mold metallurgical behavior coupled with EMS. The distribution of electromagnetic intensity in the mold is measured by Gauss meter, and the result is presented in Figure 5.

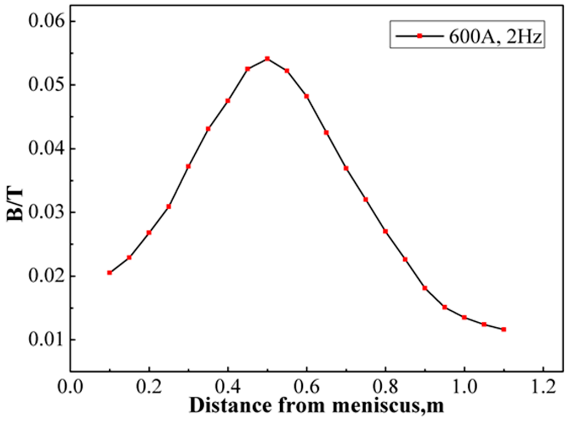

Figure 5. The distribution of measured electromagnetic intensity in the mold.

3.3.1. Water Model Experiment

A Water model experiment is useful to investigate fluid flow phenomena and helpful for the guidance of quality improvement and process parameter optimization throughout the continuous casting process. The detailed information about the experiment theory, procedure and device can be found elsewhere [25]. In this paper, the water model experiment (ratio 1:1) under three SEN conditions without EMS are conducted, and the experiment results of turbulent flow under different SEN conditions are present in Figure 6. In the water experiment, the molds are filled with transparent water in the initial stage, then the liquid with blue tracer is poured into the mold through different SEN conditions. The flow pattern at the early stage of pouring process now can be easily tracked. The level heights of four key positions on the free surface during the water experiment are detected to characterize the level fluctuation under different SEN conditions. The key positions are at center of narrow face (1#), nearby the nozzle (2#), mold corner (3#), and center of wide face (4#), respectively. The results of average level fluctuations at these positions under different SEN conditions are listed in Table 4. Compared with A-type SEN, the impact effect of jet flow on the narrow face is reduced through the B-type SEN with orthogonal installation, but a significant impact on wide face is formed. This means B-type SEN with orthogonal installation may alleviate the uneven growth of solidifying shell around the narrow side, but cause the non-uniform shell at the wide side near the impingement zone. The level fluctuations under B-type SEN with orthogonal installation apparently decrease at 1#, 2# and 3# positions, but increase to 0.5 mm at 4# position. When changing the four-port SEN to diagonal installation, the level fluctuations at 1#, 2# and 4# positions are small, but would lead to a higher fluctuation at the mold corner (0.7 mm). The level behavior is more acceptable than the other two conditions. The impingement effect of jet flow to both narrow and wide faces can be limited, and the uniform growth of solidifying shell at both wide and narrow side may be obtained by this SEN condition. However, the detailed behavior of solidifying shell under different SEN conditions should be further investigated by numerical method.

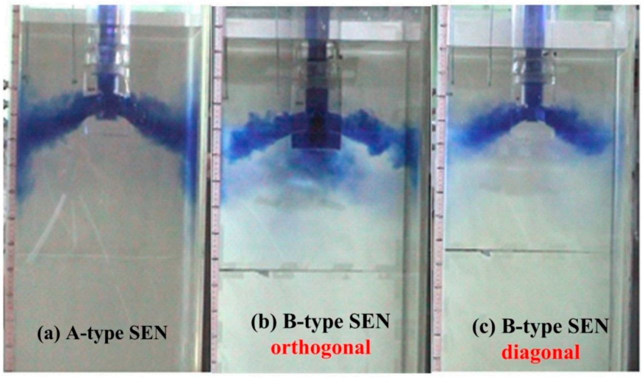

Figure 6. Water model experiment results under different SEN conditions.

Table 4. The average level fluctuations at four positions under different SEN conditions.

SEN Conditions	**Level Height, mm**			
	1#	**2#**	**3#**	**4#**
A-type SEN	1.2	1.0	1.1	0.2
B-type SEN orthogonal	0.8	0.7	0.5	0.5
B-type SEN diagonal	0.2	0.2	0.7	0.4

3.3.2. Flow Validation

The simulation result of flow pattern under the four-port SEN with orthogonal installation is verified by water model experiment under the same SEN condition. Figure 7 shows the comparison of water simulation and numerical modeling results at an early stage of the pouring process. It can be seen that the simulated flow pattern is basically consistent with the flow path and distribution of water with blue tracer, which means that it is feasible to analyze the influence of different nozzle structures and installation methods on the metallurgical behavior in the mold by numerical simulation.

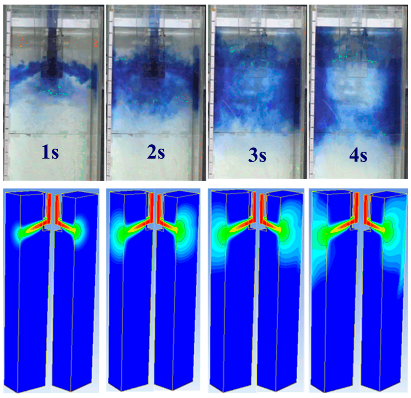

Figure 7. Comparison of water simulation and numerical modeling results.

4. Simulation Results and Discussion

The effects of two kinds of SENs and installation methods for four-port SEN on the level fluctuation, turbulent flow, heat transfer, and initial solidification in the CC mold zone are also investigated by numerical simulation. All the simulation cases are performed with mold EMS (600 A, 2 Hz), by which the rotational flow field is formed in the mold zone and the shock pressure on the mold wall can be lightened. This is beneficial to inclusion floatation and improvement of heat transfer, reducing the impacting depth of the poured steel [26].

4.1. Turbulent Flow

Figure 8 shows the velocity contour and vector at the symmetric x-z plane ($y = 0$) for A-type SEN (a), B-type SEN with orthogonal installation (b), and at the diagonal plane for B-type SEN with diagonal installation (c). The velocity contour and vector at four different x-y planes (bloom cross sections) under the three cases are also presented in Figure 8 to visually display the different methods of steel injection, which are $z = 0$ m at free surface, $z = 0.234$ m at the nozzle outlets center, $z = 0.42$ m at the EMS center, and $z = 0.7$ m at mold outlet, respectively. To conveniently describe the simulation conditions and results, the three cases are named as Case A for two-port SEN, Case B for four-port SEN with orthogonal installation and Case C for four-port SEN with diagonal installation. Figure 9 shows the three-dimensional level fluctuations under the different cases, in which the plane of steel volume fraction value 0.5 is chosen to express the status of level fluctuation.

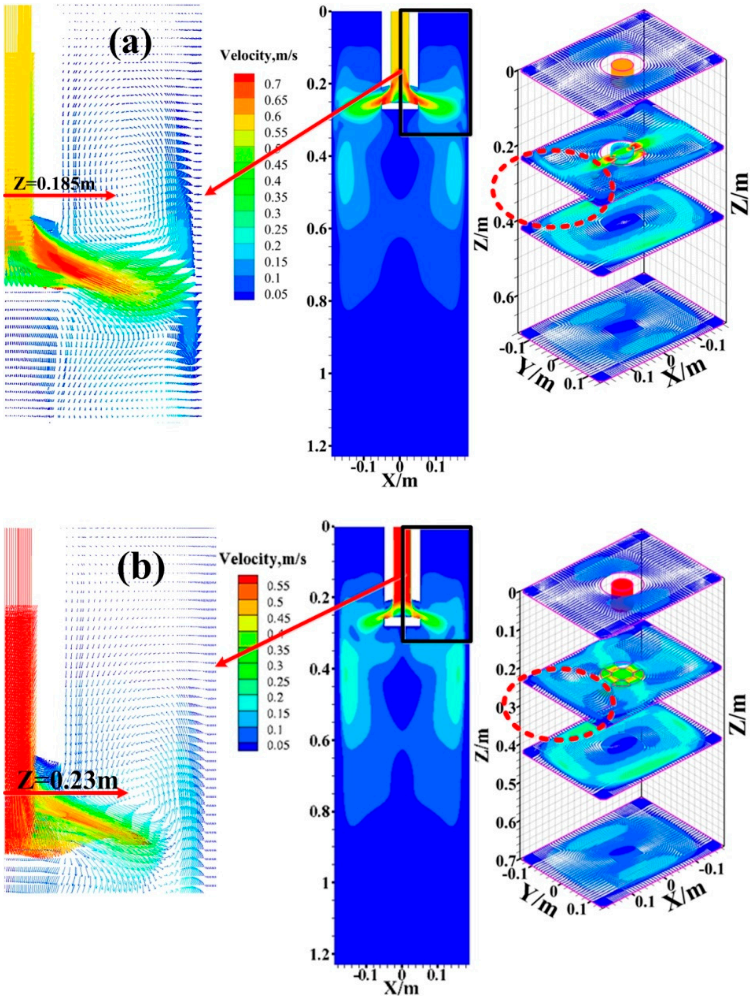

Figure 8. *Cont.*

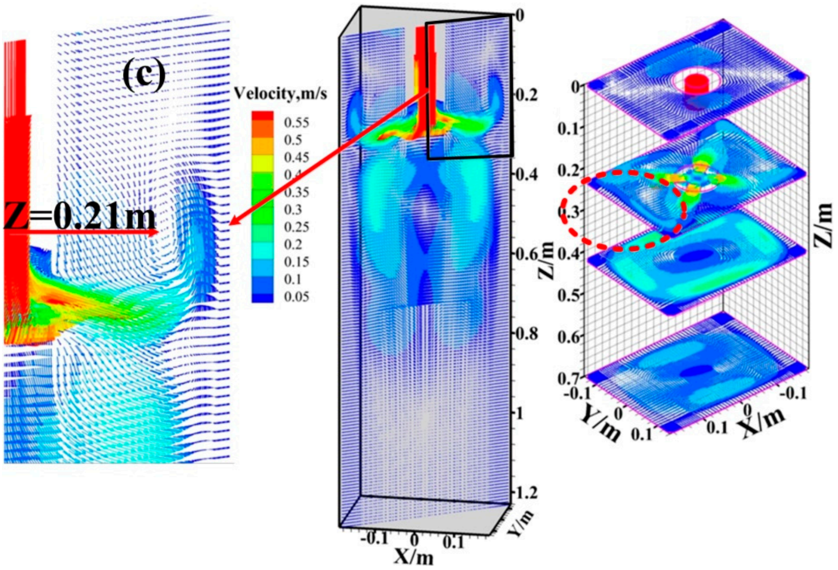

Figure 8. Velocity contour and vector at the symmetric *x*-*z* plane ($y = 0$) for Case A with A-type SEN (**a**), Case B with B-type SEN with orthogonal installation (**b**), and at diagonal plane for Case C with B-type SEN with diagonal installation (**c**).

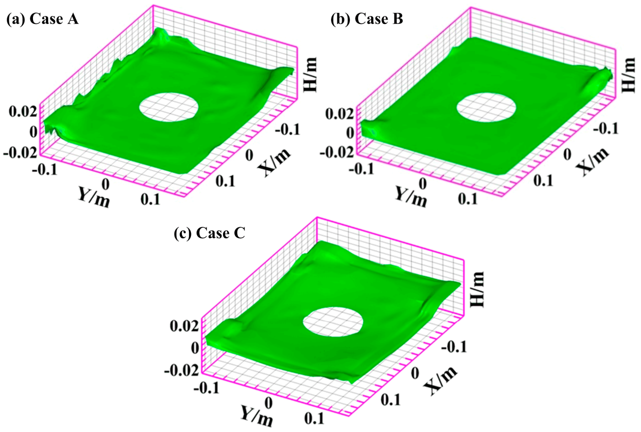

Figure 9. (**a**–**c**) The comparison of three-dimensional level fluctuations in the mold for different cases.

It can be intuitively seen from the $z = 0.234$ m planes under different cases that the impingement effect of jet flow on the mold wall differs from each other. The strong velocity at the center of narrow sides but without impingement on the wide sides for Case A, the remarkable impingement effect on both wide and narrow sides for Case B, and the feeble impingement and velocity around the center of both wide and narrow sides for Case C, respectively. The velocity field difference is gradually reduced along the casting direction and turned to swirling flow by the effect of EMS. The velocity of molten steel feeding into the mold through A-type SEN is about 0.75 m/s and 0.15 m/s larger than B-type SEN. This may cause a higher shock pressure of the narrow face in the mold, then forms a larger and stronger circular flow upon the impacting point, which can easily induce the severe fluctuation of the free surface. This also increases the chance of slag entrapment. The center of circulations upon the impacting point in Case A and Case B is 0.185 m and 0.23 m, and the big range and quantity of level fluctuation in Case A is more obvious than in Case B. For the Case B and Case C having the same structure of SEN, but with different installation methods, the flow velocity of molten steel injected from the nozzle outlets are the same. An installation method such as Case C can increase the distance between the nozzle outlets and mold wall, which means low shock velocities on mold corner walls, and less shock pressure of liquid steel to the mold wall. For Case C, the flow intensity of upper circulation with the center at approximately 0.21 m below the meniscus is weak, which may reduce the level fluctuation. The highest level fluctuations for the three cases are 11.5 mm, 9.5 mm and 5.5 mm, respectively. In local regions, the maximum height of level fluctuation in Case A and Case B is much higher than Case C, which may easily lead to damage of the steel/slag interface and slag entrainment. The largest value of level fluctuation under Case C is acceptable for the movement of slag, which happens at four corners of the mold free surface due to the circular flow. Therefore, the range of level fluctuation and chance of slag entrapment can be reduced under Case C.

4.2. Temperature Field and Solidification

Figure 10 presents the liquid fraction distribution at various cross sections of x-y planes and x-z plane ($y = 0$) for the three cases. Figure 11 shows the growth of shell thickness at the x-z planes (a) and y-z planes (b) along the casting direction under different SEN conditions. The results of solidified shell behavior show that the solidifying shell increases non-uniformly at the cross section of the x-z plane but uniformly at the y-z plane along the casting direction under A-type SEN due to a lack of flow impingement on the shell of mold wide face. It is worth noting impingement on the narrow face, which can stunt the growth of the solidifying shell near the impacting zone. The thickness of solidified shell at narrow side decreases from 2.78 mm at around 0.2 m below the meniscus to 1.67 mm at 0.35 m below meniscus, while the shell at wide side grows uniformly. The similar phenomenon of solidifying shell growth can also be observed in Case B, in which the four outlets of the nozzle are perpendicular to the mold walls, the uneven phenomenon of the solidifying shell growth at x-z plane is mostly eliminated, because of the lower outlet velocities of molten steel and lower shock pressure on the mold narrow face compared with Case A. But the solidifying shell at the y-z plane has an uneven growth in the flow impacting zone because the distance from nozzle outlets to the mold wide face is 50 mm shorter than to the narrow face. The thickness of solidified shell at wide side increases from 4.92 mm at 0.2 m below the meniscus to 5.82 mm at 0.32 m below the meniscus, which is thicker than other two cases. The thickness of solidified shell at the width direction of mold outlet ($z = 0.7$ m) and computational outlet ($z = 1.23$ m) under Case B are 14.28 mm and 26.13 mm respectively, which is about 3.3 mm and 1.51 mm thicker than Case A, respectively. While the thickness of solidified shell at the thickness direction of mold outlet and computational outlet under Case B are 13.98 mm and 26.05 mm, which is about 1.92 mm and 0.81 mm thinner than Case A. Compared with Case B, Case C increases the distance of jet flow to mold wall by changing the installation method of four-port SEN from orthogonal to diagonal, which has a great effect on decreasing the shock pressure on the wall, lowering the level fluctuation range and reducing the chance of slag entrapment. The thickness of solidified shell at mold outlet ($z = 0.7$ m) is 15.43 mm at width direction and 14.02 mm at thickness direction, respectively. It increases to 26.65 mm at width direction and 26.16 mm at thickness direction for the computational outlet ($z = 1.23$ m). The results of Figures 10 and 11 show that the solidifying shell increase gradually and uniformly along the casting direction under Case C at both x-z plane and y-z plane due to a lack of flow impingement on the four surfaces of mold on the corner wall. Less shock pressure to the mold wall leads to small effect on the uniformity of solidifying shell. Therefore, the growth behavior of solidifying shell in the bloom mold under the four-port SEN with diagonal installation is more acceptable than the other two cases, and can reduce the risk of surface cracks and liquid breakout.

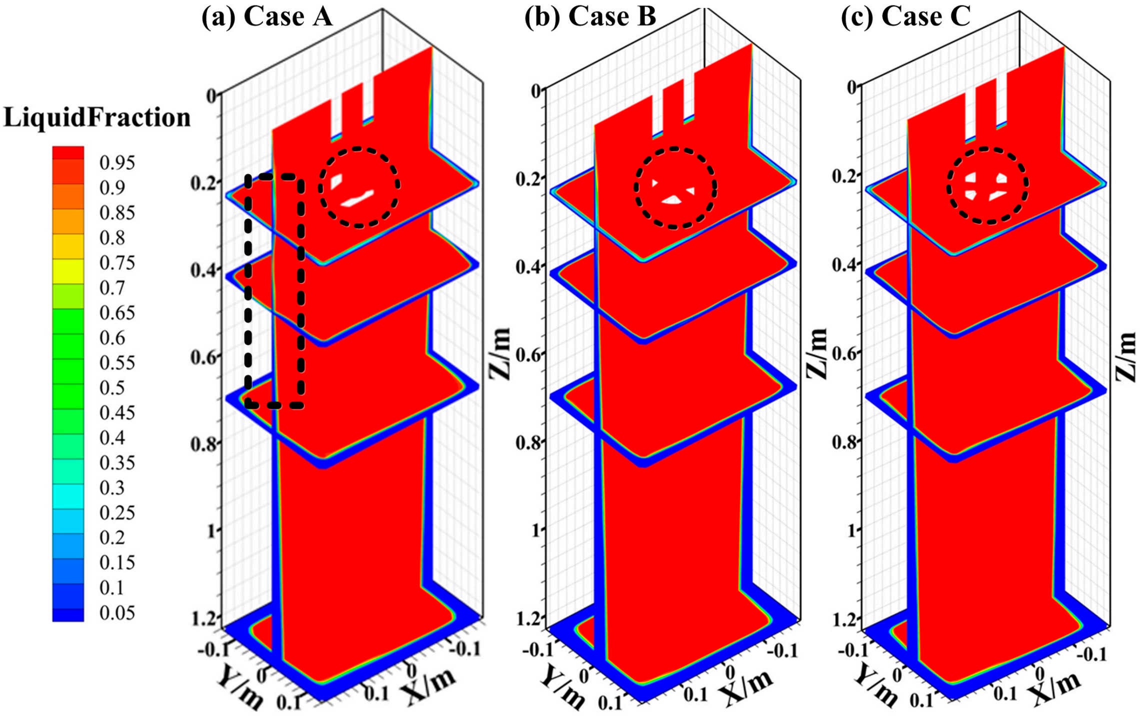

Figure 10. (**a**–**c**) Liquid fraction distribution at various cross sections and *x*-*z* plane for different cases.

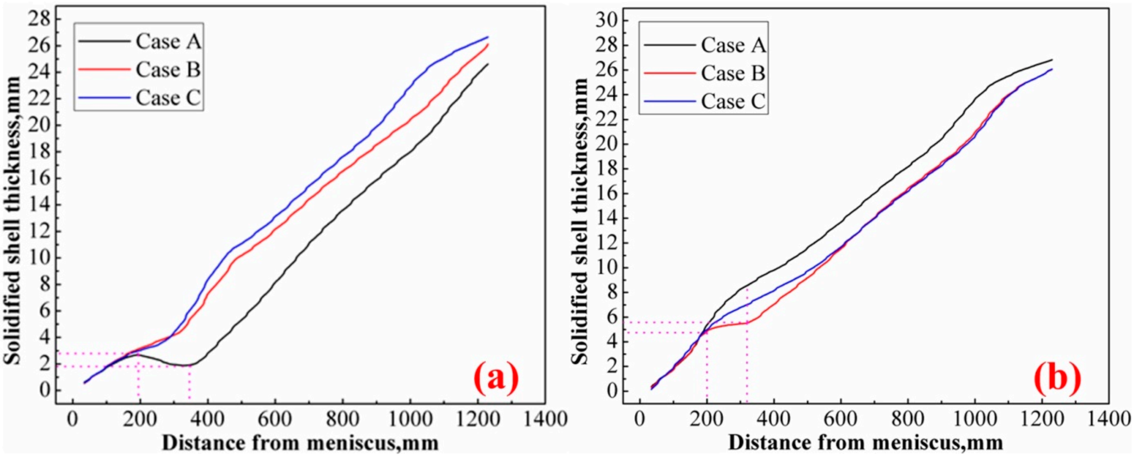

Figure 11. Shell thickness distributions at the *x*-*z* plane (**a**) and *y*-*z* plane (**b**) along the casting direction for the three cases.

Figure 12 shows the temperature variation at the centerline of the mold corner (dashed line) and the centerline of the bloom wide face (solid line) along the casting direction for three different cases. The results show that the surface and corner temperature of the bloom upon the injection impacting zone has the same variation under different cases, but the downward trend of surface temperature under Case B has been changed when the bloom reaches the impacting zone. There is a smaller increase, then the surface temperature continues to decrease after the bloom is pulled out of the region. The wide surface temperature at mold outlet (z = 700 mm) under Case A, Case B and Case C are 1310 K, 1344 K and 1326 K, respectively. Then, the temperature in all cases rises to 1345 K at the computational outlet (z = 1230 mm) because of the change of heat transfer condition from mold region to secondary cooling zone. The reason for the mold corner temperature variation around the impacting zone under Case C is similar to the wild wall surface temperature variation under Case B. The impacting location of the Case C is on the mold corner. The corner temperature at the mold outlet for the three cases are

1150 K, 1146 K and 1183 K, which means that Case C is less likely to cause the corner crack on the continuous casting bloom. The corner temperature at computational outlet rises to approximately 67 K, 81 K and 21 K to 1217 K, 1227 K and 1202 K at the secondary cooling zone (z = 700 mm–1230 mm). A lower temperature increase means less chance to cause the longitudinal corner crack of the continuous casting bloom. The temperature difference of corner and wide surface at mold outlet under these three cases are 160 K, 198 K and 143 K respectively, a low temperature difference between the bloom surface and corner along the casting direction can be observed under the Case C. This means less chance to form transverse cracks of the steel. To avoid repetition, the temperature variation at narrow face under three cases along the casting direction is not described in this paper, because the variation is similar to the wide surface, where the temperature at impingement zone of narrow surface also has a sudden rise under Case A due to the strong impact to the wall.

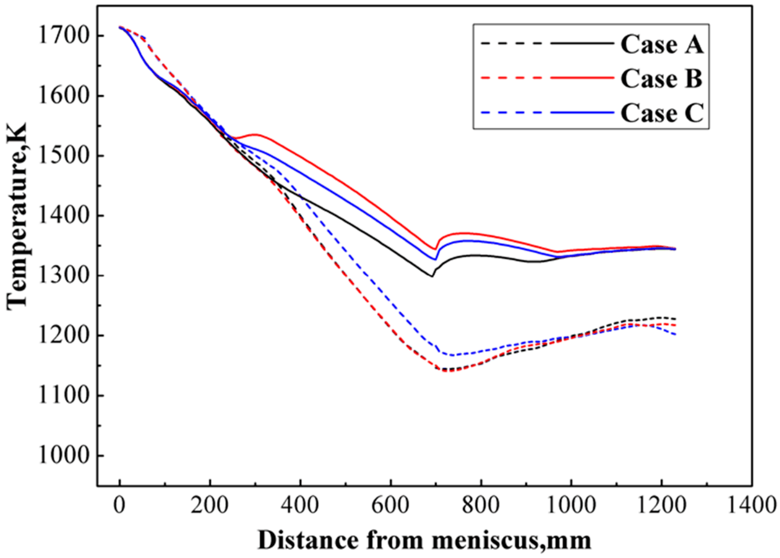

Figure 12. Temperature variation at centerline of mold corner (dashed line) and bloom wide face (solid line) along the casting direction for three different cases.

By comprehensively considering and comparing the results of Case A, Case B and Case C, the results of flow pattern, level fluctuation and solidification behavior in the computational zone under Case C are more likely to fulfill the requirements for the quality of mold metallurgical behavior for bloom casting.

5. Conclusions

The water model experiments with different SENs were conducted, and the effects of SENs on the flow pattern, temperature field, and solidification behavior in the mold of heavy railway steel were calculated and compared by FLUENT 14.5 (FLUENT Inc., New York, NY, USA). The main conclusions of this paper are summarized as follows:

(1) Water model simulation results illustrate that four-port SEN with diagonal installation can alleviate the impingement effect of jet flow both on the narrow and wide face, which may be beneficial to the uniform growth of solidifying shell.

(2) When using the four-port SEN with diagonal installation, the maximum level fluctuation can be reduced to 5.5 mm, compared with two-port SEN and four-port SEN with orthogonal installation of which is 11.5 mm and 9.5 mm respectively, and the shock pressure of the injecting flow to the mold wall can be lightened because of low injecting velocity and long impacting distance to the wall.

(3) When using the four-port SEN with diagonal installation, the temperature trend at both wide and narrow surfaces is more acceptable compared with two-port SEN or four-port SEN with orthogonal installation. The corner temperature in the mold zone is about 30 K higher because of the liquid steel impacting effect on the mold corner.

(4) Compared with two-port SEN or four-port SEN with orthogonal installation, local solidified shell thinning phenomenon on both wide and narrow sides is eliminated under four-port SEN with diagonal installation due to a lack of impingement of jet flow.

Acknowledgments: The authors would like to express their gratitude for the financial support by the National Natural Science Foundation of China (51471122) and the Key program of Natural Science Foundation of Hubei Province of China (2015CFA128).

Author Contributions: Hongwei Ni and Hua Zhang conceived and designed the study. Qing Fang performed the experiments and simulations. Bao Wang contributed to the result analysis and paper preparation. Qing Fang and Zean Lv wrote the manuscript.

Conflicts of Interest: The authors declare no conflict of interest.

References

1. Thomas, B.G.; Zhang, L. Mathematical modeling of fluid flow in continuous casting. *ISIJ Int.* **2001**, *41*, 1181–1193. [CrossRef]
2. Xu, M.G.; Zhu, M.Y. Transport phenomena in a beam-blank continuous casting mold with two types of submerged entry nozzle. *ISIJ Int.* **2015**, *55*, 791–798. [CrossRef]
3. Zhang, L.L.; Chen, D.F.; Long, M.J.; Chen, H.B.; Huang, Y.W.; Dong, Z.H. Study on the fluid flow in a semi-open-stream-poured beam blank continuous casting mold with submerged refractory funnels by multiphase modeling. *Metals* **2016**, *6*, 104. [CrossRef]
4. Barreto, J.D.; Morales, R.D.; Garcia-Hernandez, S.; Najera-Bastida, A.; Calderon-Ramos, I. Modeling study of molten steel turbulence control by SEN design improvement in a conventional slab caster. *Steel Res. Int.* **2014**, *86*, 517–527. [CrossRef]
5. Calderón-Ramos, I.; Morales, R.D. The role of submerged entry nozzle port shape on fluid flow turbulence in a slab mold. *Metall. Mater. Trans. B* **2015**, *46*, 1314–1325. [CrossRef]
6. Li, D.W.; Su, Z.J.; Marukawa, K.; He, J.C. Simulation on effect of divergent angle of submerged entry nozzle on flow and temperature fields in round billet mold in electromagnetic swirling continuous casting process. *J. Iron Steel Res. Int.* **2014**, *21*, 159–165. [CrossRef]
7. Liu, K.; Ren, Z.; Feng, L. Simulation study of heat transfer and solidification in the mold of bloom continuous caster. *Metal. Int.* **2013**, *18*, 26–28.
8. Shen, J.L.; Chen, D.F.; Xie, X.; Zhang, L.L.; Dong, Z.H.; Long, M.J.; Ruan, X.B. Influences of SEN structures on flow characters, temperature field and shell distribution in 420 mm continuous casting mould. *Ironmak. Steelmak.* **2013**, *40*, 263–275. [CrossRef]
9. Wu, D.F.; Cheng, S.S.; Zhao, J.J. Performance comparison of three kinds of submerged entry nozzles for bloom mold. *J. Iron Steel Res. Int.* **2008**, *15*, 315–321.
10. Dang, A.G.; Cui, J.; Liu, J.J.; Feng, Y. Effect of muitihole nozzle on flow field and temperature field of liquid in mold for casting bearing steel 280 mm × 325 mm bloom. *Spec. Steel* **2016**, *37*, 12–15. (In Chinese).
11. Sun, H.B.; Li, L. Application of swirling flow nozzle and investigation of superheat dissipation casting for bloom continuous casing. *Ironmak. Steelmak.* **2016**, *43*, 228–233. [CrossRef]
12. Sun, H.B.; Zhang, J.Q. Macrosegregation improvement by swirling flow nozzle for bloom continuous castings. *Metall. Mater. Trans. B* **2014**, *45*, 936–946. [CrossRef]
13. Ren, B.Z.; Chen, D.F.; Wang, H.D.; Long, M.J.; Han, Z.W. Numerical simulation of fluid flow and solidification in bloom continuous casting mould with electromagnetic stirring. *Ironmak. Steelmak.* **2015**, *42*, 401–408. [CrossRef]
14. Ren, B.Z.; Chen, D.F.; Wang, H.D.; Long, M.J. Numerical analysis of coupled turbulent flow and macroscopic solidification in a round bloom continuous casting mold with electromagnetic stirring. *Steel Res. Int.* **2015**, *86*, 1104–1115. [CrossRef]

15. Hrenya, C.M.; Bolio, E.J.; Chakrabarti, D.; Sinclair, J.L. Comparison of low Reynolds number k-ε turbulence models in predicting fully developed pipe flow. *Chem. Eng. Sci.* **1995**, *50*, 1923–1941. [CrossRef]
16. *FLUENT 6.2-Theory Guide*; Fluent Inc.: Lebanon, NH, USA, 2005.
17. Spitzer, K.H.; Dubke, M.; Schwerdtfeger, K. Rotational electromagnetic stirring in continuous casting of round strands. *Metall. Mater. Trans. B* **1986**, *17*, 119–131. [CrossRef]
18. Poirier, D.R. Permeability for flow of interdendritic liquid in columnar-dendritic alloys. *Metall. Mater. Trans. B* **1987**, *18*, 245–255. [CrossRef]
19. Deng, A.Y.; Xu, L.; Wang, E.G.; He, J.C. Numerical analysis of fluctuation behavior of steel/slag interface in continuous casting mold with static magnetic field. *J. Iron Steel Res. Int.* **2014**, *21*, 809–816. [CrossRef]
20. Wang, W.W.; Zhang, J.Q.; Chen, S.Q.; Dong, J.M. Effect of nozzle outlet angle on the fluid flow and level fluctuation in a bloom casting mould. *J. Univ. Sci. Technol. Beijing* **2007**, *29*, 816. (In Chinese).
21. Lai, K.Y.M.; Salcudean, M.; Tanaka, S.; Guthrie, R.I.L. Mathematical modeling of flows in large tundish systems in steelmaking. *Metall. Mater. Trans. B* **1986**, *17*, 449–459. [CrossRef]
22. Alizadeh, M.; Jenabali, J.A.; Abouali, O. A new semi-analytical model for prediction of the strand surface temperature in the continuous casting of steel in the mold region. *ISIJ Int.* **2008**, *48*, 161–169. [CrossRef]
23. Park, J.K.; Thomas, B.G.; Samarasekera, I.V. Analysis of thermomechanical behaviour in billet casting with different mould corner radii. *Ironmak. Steelmak.* **2002**, *29*, 359–375. [CrossRef]
24. Morales, R.D.; Pez, A.G.; Olivares, I.M. Heat transfer analysis during water spray cooling of steel rods. *ISIJ Int.* **1990**, *30*, 48–57. [CrossRef]
25. Li, B.; Tsukihashi, F. Vortexing flow patterns in a water model of slab continuous casting mold. *ISIJ Int.* **2005**, *45*, 30–36. [CrossRef]
26. Fang, Q.; Ni, H.W.; Wang, B.; Zhang, H.; Ye, F. Effects of EMS Induced Flow on Solidification and Solute Transport in Bloom Mold. *Metals* **2017**, *7*, 72. [CrossRef]